physica status solidi a
www.pss-a.com

A Combination of Ion Implantation and High-Temperature Annealing: The Origin of the 265 nm Absorption in AlN

Lukas Peters, Christoph Margenfeld,* Jan Krügener, Carsten Ronning, and Andreas Waag*

The commonly observed absorption around 265 nm in AlN is hampering the outcoupling efficiency of light-emitting diodes (LEDs) emitting in the UV-C regime. Carbon impurities in the nitrogen sublattice (C_N) of AlN are believed to be the origin of this absorption. A specially tailored experiment using a combination of ion implantation of boron, carbon, and neon with subsequent high-temperature annealing allows to separate the influence of intrinsic point defects and carbon impurities regarding this absorption. Herein, the presented results reveal the relevance of the intrinsic nitrogen-vacancy defect V_N. This is in contradiction to the established explanation based on C_N defects as the defect causing the 265 nm absorption and will be crucial for further UV-LED improvement. Finally, in this article, a new interpretation of the 265 nm absorption is introduced, which is corroborated by density functional theory (DFT) results from the past decade, which are reviewed and discussed based on the new findings.

1. Introduction

In the past decades, light-emitting diodes (LEDs) based on group III-Nitride semiconductors changed the way we are illuminating the world. Blue light from GaN LEDs is partially converted into yellow light, leading to white emitting LEDs with efficacies of over 200 lumen per Watt. In addition to the highly optimized blue-emitting LEDs, emitters for the UV range received great interest lately. In terms of efficiency, LEDs emitting in the UV-B and UV-C regimes are lagging behind their blue and UV-A pendants, due to physical restrictions as well as technological challenges that have to be surpassed to achieve higher efficiencies. Those challenges comprise the threading dislocation density (TDD) and transparency of the AlN growth substrate or template, light outcoupling, doping, and point defect control, as well as processing challenges due to excessive wafer bow caused by differences in thermal expansion coefficients between LED stack and substrate.

L. Peters, C. Margenfeld, A. Waag
Institute of Semiconductor Technology
Technische Universität Braunschweig
Hans-Sommer-Straße 66, D-38106 Braunschweig, Germany
E-mail: lukas.peters@tu-braunschweig.de; c.margenfeld@tu-braunschweig.de

L. Peters, C. Margenfeld, A. Waag
Laboratory for Emerging Nanometrology (LENA)
Technische Universität Braunschweig
Langer Kamp 6, D-38106 Braunschweig, Germany

J. Krügener
Institute for Electronic Materials and Devices
Leibniz Universität Hannover
Schneiderberg 32, D-30167 Hannover, Germany

C. Ronning
Institute of Solid State Physics
Friedrich Schiller University of Jena
Max-Wien-Platz 1, D-07743 Jena, Germany

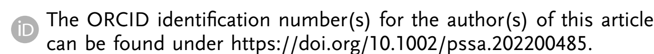
The ORCID identification number(s) for the author(s) of this article can be found under https://doi.org/10.1002/pssa.202200485.

© 2022 The Authors. physica status solidi (a) applications and materials science published by Wiley-VCH GmbH. This is an open access article under the terms of the Creative Commons Attribution License, which permits use, distribution and reproduction in any medium, provided the original work is properly cited.

DOI: 10.1002/pssa.202200485

UV-C LEDs for disinfection/sterilization purposes exhibit the largest germicidal efficacy around an emission wavelength of 265 nm.[1] Coincidentally, AlN—being one of the key components of such UV LEDs—possesses a prominent absorption line at a photon wavelength of 265 nm (corresponding to ≈4.7 eV photon energy). This is closely linked to the incorporation of excessive amounts of carbon into the crystal during its growth, according to the existing literature.[2–5] In this study, we will amend this interpretation and put forward an experiment that suggests the currently dominating interpretation of the 265 nm absorption line may be incomplete. Based on our data, the role of the nitrogen vacancy and the interplay between this intrinsic defect and carbon impurities have to be revised. These insights open the door for further improvement of UV LEDs.

Indeed, carbon is incorporated unintentionally as an impurity during crystal growth and often stems from source materials such as MO precursors (in metal–organic vapor phase epitaxy, MOVPE) or powders (in physical vapor transport, PVT), as well as reactor components such as crucibles or susceptors. Even though to a certain extent, carbon contamination can be influenced by the growth conditions such as temperature, supersaturation, V/III ratio, and pressure,[6] as well as by the crystal orientation[7] and reactor design, it is challenging to fully suppress carbon incorporation in MOVPE and PVT growth of AlN crystals.

Carbon acts as an amphoteric dopant in AlN depending on the lattice site that it is incorporated on.[8] The deep UV absorption band at ≈4.7 eV (265 nm) is until now believed to be caused by carbon on nitrogen sites (C_N), which act as an acceptor.[9] With a

high concentration of electrically active acceptors at growth temperature, the Fermi level shifts toward the valence band, generally favoring the formation of compensating donors. Apart from extrinsic donor-type impurities such as oxygen[5,10,11] and silicon,[12] the compensation of C_N acceptors by the incorporation of nitrogen vacancies (V_N) as shallow donors has been reported in PVT growth.[8] The occurrence of a high concentration of nitrogen vacancies and carbon impurities seems to go hand in hand, which is a typical behavior for compensation. Presently, the attribution of the absorption band at ≈4.7 eV to carbon on nitrogen sites seems to be the consensus in the literature, whereas the consequent formation of nitrogen vacancies due to compensation has not been explored rigorously.[2,4,5] Recently, the overall interpretation has already been challenged by Jin et al. who conducted annealing experiments on bulk crystals. They observed a decrease of the ≈4.7 eV absorption after annealing, whereas SIMS measurements even showed a small increase in carbon concentration after annealing. Nitrogen vacancies are instead proposed as a possible cause of the absorption band.[13]

To deepen the understanding of the ≈4.7 eV absorption band in AlN, we present the results of a tailored experiment using ion implantation followed by high-temperature annealing (HTA) of AlN thin films on sapphire that allows us to decouple the effects from the incorporation of carbon and nitrogen vacancies. Implantation into pure materials has two effects: First, it can provide a very controlled impurity concentration (i.e., carbon) spanning multiple orders of magnitude without relying on indirect control through tuning growth conditions. Second, the impact of high-energy ions leads to a plethora of native point defects, mostly Frenkel pairs of vacancy and interstitial, which are generated when atoms are displaced from a lattice site into an interstitial position. While Frenkel pair generation is more probable for the nitrogen sublattice, AlN is in general exceptionally resilient to irradiation with high-energy particles.[14] Defect self-recombination (or dynamical annealing), which takes place when high-energy ions knock back atoms onto their respective lattice sites during implantation, is reported to be very efficient in heavily irradiated AlN crystals, leading to very high threshold fluences for amorphization, in fact making full amorphization almost impossible to occur.[15] Consequently, no randomly oriented crystalline domains or dislocation loops/localized stacking faults were observed in implanted AlN.[16] Due to this, AlN crystals with a high concentration of native point defects can be obtained by ion implantation without reaching the limit for amorphization or inducing any unwanted structural defects that may obfuscate the optical properties. Only because of the discussed resilience to irradiation, AlN is suited for the herein-discussed experiment since high levels of ion fluences are needed to observe the distinct absorption band in thin films.

Recently, the recrystallization of several 100 nm thick AlN/sapphire templates using HTA has gained a lot of interest as a means of manufacturing epitaxial layers with a very high crystallinity. First introduced by Fukuyama et al., who employed an N_2–CO atmosphere to prevent decomposition at high annealing temperatures of up to 1700 °C,[17] the HTA technique has been developed further by Miyake et al. using the so-called face-to-face-approach.[18] Apart from reducing the dislocation density of AlN thin films, we apply the HTA technique in this study to fully recover the implantation damage. Since the defect recombination of Frenkel pairs has been reported to largely occur at temperatures below ≈1400 °C,[19] a very high degree of recovery of irradiation-induced crystal damage can be assumed after annealing at 1700 °C. Therefore, intrinsic point defects can be expected to dominate the optical properties before annealing, whereas optical properties will be controlled by implanted impurities after annealing. The experiments reported here have been designed in a way that this separation leads to a deeper insight into the origin of the 265 nm absorption band in AlN.

To observe these differences before and after annealing, though, the AlN starting material has to exhibit a high degree of transparency, i.e., low initial concentration of optically active point defects prior to the implantation. Physical vapor deposited (PVD) AlN films fulfill these requirements.

Here, we report on a systematic investigation of absorbance spectra for samples implanted with varying fluences of carbon and two reference species (neon, boron) before and after HTA. The ion fluence and ion energy of both, boron and neon have been chosen to lead to comparable defect distributions after implantation. In comparison to carbon, boron is an isoelectronic group III species and neon does not form any chemical bonds in AlN and likely diffuses out of the lattice upon annealing. Comparing these six types of samples (boron, carbon, and neon implanted before and after HTA) allows us to obtain new information on the origin of the absorption band at 265 nm. Our results discussed in more detail below suggest that the interpretation of C_N being the sole cause of the ≈4.7 eV absorption band in AlN may be incomplete. Based on our experimental insights, the involvement of nitrogen vacancies as compensating donors in the formation of the ≈4.7 eV absorption band in AlN should be reconsidered. Our comprehensive model is fully compatible with experimental results and principally compatible with theoretical calculations of formation energies (density functional theory, DFT) published by other groups to date.

2. Results and Discussions

Due to the similar atomic masses of boron, carbon, and neon, the implantation damage, like displacement per atom (dpa) and the concentration of defects as a function of ion energy and also the implantation profiles, are quite comparable (see **Figure 1**a). Since neon has a higher atomic mass than boron and carbon, the damage profile for neon shows a high-energetic tail, as shown in Figure 1b (blue curves). The normalized vacancy concentration was calculated using displacement energies of aluminum and nitrogen obtained from ab initio molecular dynamics simulations reported by Xi et al.[14] ($E_{D,Al} = 94.1$ eV and $E_{D,N} = 38.8$ eV). As a result, a vacancy ratio of approximately $[V_N]/[V_{Al}] = 2.4$ has been obtained. The calculated damage profile for boron implantation using $E = 40$ keV yields peak V_N concentrations ≈50 times higher than the peak boron concentration (excluding dynamical annealing during implant at room temperature). If one takes the atomic sublattice density and the peak V_N concentrations into account, amorphization is expected to occur for ion fluences greater than $\approx 7 \times 10^{15}\ \text{cm}^{-2}$, cf. Figure 1b marked in purple (V_N concentrations equals the atomic density of the N-sublattice).

© 2022 The Authors. physica status solidi (a) applications and materials science published by Wiley-VCH GmbH
18626319, 0, Downloaded from https://onlinelibrary.wiley.com/doi/10.1002/pssa.202200485 by Cochrane Germany, Wiley Online Library on [11/05/2023]. See the Terms and Conditions (https://onlinelibrary.wiley.com/terms-and-conditions) on Wiley Online Library for rules of use; OA articles are governed by the applicable Creative Commons License

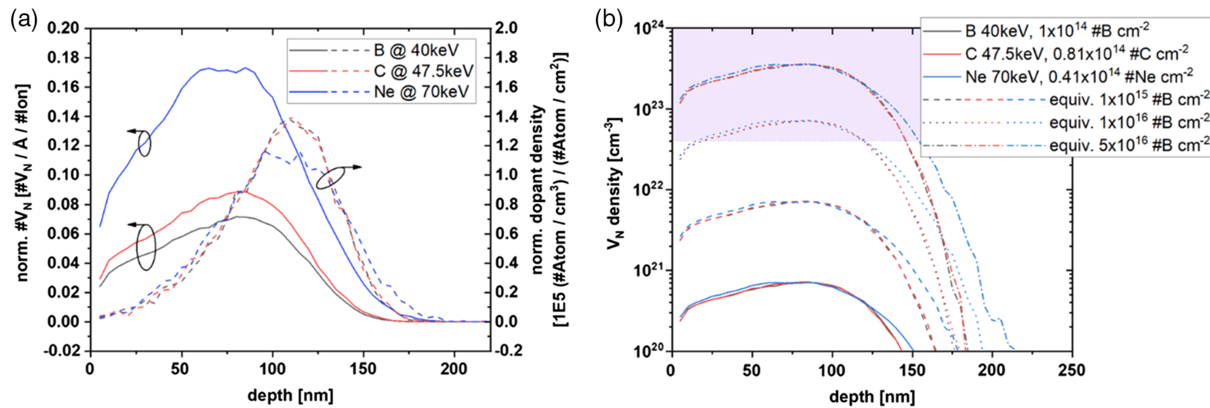

Figure 1. a) Normalized depth distributions of the implanted ions (dotted lines) and V_N defects (solid lines), as calculated by TRIM simulations. b) Calculated V_N density for varying ion fluences. In purple: Theoretical amorphization threshold for AlN.

Table 1. Sample overview of the three different implantation series and the used parameters.

B series sample names	Fluence at 40 keV [cm^{-2}]	C series sample names	Fluence at 47.5 keV [cm^{-2}]	Ne series sample names	Fluence at 70 keV [cm^{-2}]
B1E14	1×10^{14}	C1E14	0.81×10^{14}	Ne1E14	0.41×10^{14}
B1E15	1×10^{15}	C1E15	0.81×10^{15}	Ne1E15	0.41×10^{15}
B1E16	1×10^{16}	C1E16	0.81×10^{16}	Ne1E16	0.41×10^{16}
B5E16	5×10^{16}	C5E16	4.05×10^{16}	Ne5E16	2.05×10^{16}

Respective defect concentrations for boron implantations at 40 keV with ion fluences of 1×10^{14} to 5×10^{16} cm^{-2} have, therefore, been used as reference values to cover a broad range of point defect concentrations. To match these damage profiles, carbon and neon implantation were conducted at implantation energies of 47.5 and 70 keV, respectively (see Figure 1a). The ion fluences for carbon and neon can now be adjusted to match the boron damage profiles (see Figure 1b). The respective adjustment factors are 0.41 for Ne and 0.81 for C implantations. To maintain a better overview, the neon and carbon implanted samples will be abbreviated with their equivalent boron fluence, thus, e.g., 4.05×10^{16} cm^{-2} of carbon implantation equal sample C5E16, since 5×10^{16} cm^{-2} is the boron fluence creating the same concentration of point defects in comparison to an actual fluence of 4.05×10^{16} cm^{-2} of carbon ions. All implantation parameters are listed in **Table 1**.

Even though the theoretical amorphization threshold is surpassed for the two highest ion fluences, high-resolution X-ray diffraction (HRXRD) measurements confirmed that the AlN layers remain largely monocrystalline, even at these highest ion fluences, which is in line with the strong dynamical annealing in AlN during implantation at room temperature. Nevertheless, an increasing degree of disorder is indicated by the drastically increasing diffuse scattering, leading to an increase in background signal for the peak intensities around the AlN (0002) Bragg peak for ion fluences of 1×10^{16} and 5×10^{16} cm^{-2} (see **Figure 2**). In contrast, ω-2θ scans still confirm an epitaxial orientation even for the samples with high fluences,

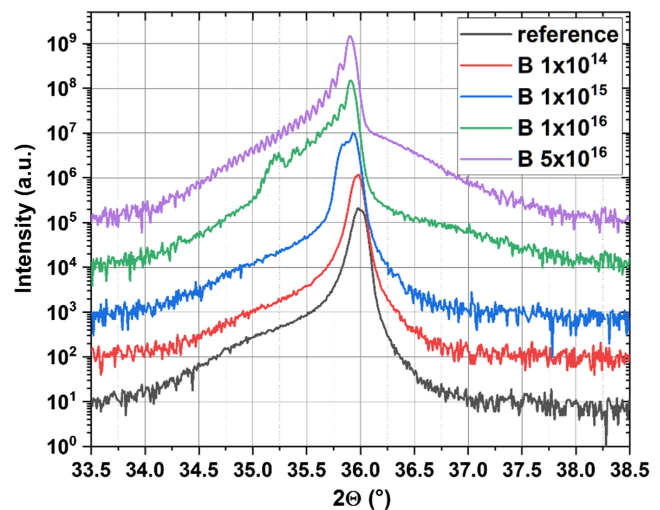

Figure 2. Coupled ω-2θ scans around the AlN (0002) reflex showing the presence of a strained layer at diffraction angles below the main Bragg peak and an increasing diffuse background due to disorder.

i.e., B1E16 to B5E16 (Figure 2). As is evident from the Bragg peak shifting to smaller 2θ angles and the observation of a shoulder on the left side of the former, an expansion of the lattice in the *c*-direction occurs, which is in line with reports from literature where an increase in lattice constant has been explained by the high density of generated Frenkel pairs, a situation which we also expect at high implantation fluence.[19] X-ray diffraction (XRD) reciprocal space maps (not shown here) confirm that the damaged layer is partially strained to the substrate and the increase in lattice constant predominantly occurs in the out-of-plane direction, i.e., *c*-direction, a behavior which contributes to the reported irradiation resilience of AlN.

After implantation, the samples showed an amber color for all fluences used in the experiment. As expected, the intensity of the coloring increases with implantation fluence. Since coloring was observed independently from the implant species, it is reasonable to assume that intrinsic point defects cause the absorption leading to the amber color. In addition, transmittance

© 2022 The Authors. physica status solidi (a) applications and materials science published by Wiley-VCH GmbH

18626319, 0, Downloaded from https://onlinelibrary.wiley.com/doi/10.1002/pssa.202200485 by Cochrane Germany, Wiley Online Library on [11/05/2023]. See the Terms and Conditions (https://onlinelibrary.wiley.com/terms-and-conditions) on Wiley Online Library for rules of use; OA articles are governed by the applicable Creative Commons License

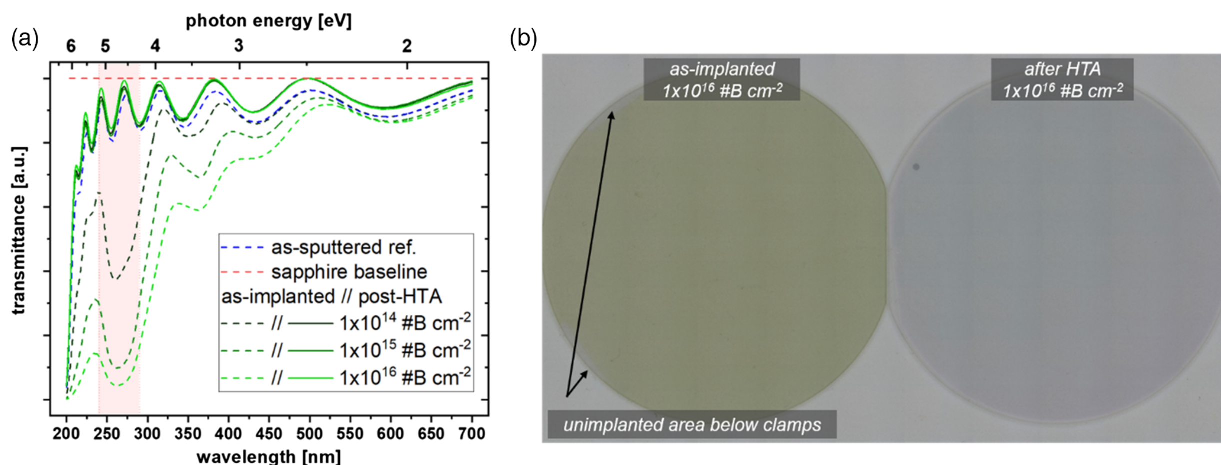

Figure 3. a) Transmittance spectra of the boron implant series before and after annealing, normalized to a bare sapphire wafer. The distinct transmittance drop in the UV-C is marked in red. b) Photograph of an as-implanted and annealed AlN/sapphire sample implanted with boron ions to an ion fluence of 1×10^{16} cm^{-2}.

measurements revealed a broad and strong decrease in the transmittance (increase in absorption) in the UV range (cf. **Figure 3**a for exemplary transmittance measurements of the samples B1E14 to B1E16). Since the broad transmittance loss of the as-implanted samples is superimposed with the thickness fringes (dashed curves in Figure 3a), the identification of defect bands is not straightforward. Nevertheless, a strong drop of transmittance around 265 nm can clearly be identified. It is this absorption that was previously attributed to carbon on nitrogen sites (C_N) by Collazo et al. in 2012.[2] This interpretation has been repeated several times and seems to be widely accepted in the AlN community up to now.[4,12,20–25] Interestingly, the broad absorption is vanishing almost completely after the HTA process (see Figure 3a). At the same time, the samples are losing their amber color, becoming fully transparent to the bare eye. A direct comparison between a boron as-implanted and annealed sample with an ion fluence of 1×10^{16} cm^{-2} is shown in the photograph in Figure 3b. The transmittance spectra after HTA for both the implanted (green solid curves) and non-implanted (blue dashed curve) sample are almost identical to each other (see Figure 3a). We conclude that HTA is a suitable tool to cure the majority of intrinsic point defects that were formed during ion implantation (i.e., Frenkel pairs). It is, therefore, justified to assume that the combination of implantation and HTA obviously leads to the incorporation of boron on metal sites in AlN without additional optically active point defects detectable by absorption measurements on such thin films.

Comparing the spectra between different implant species (boron, carbon, and neon) in the as-implanted state, as shown in **Figure 4**, the samples exhibit similar spectra independently from the implanted species, namely a strong absorption at 265 nm. This is the first indication that the 265 nm absorption line cannot be solely related to carbon but the intrinsic defects caused by ion implantation should also be considered as a potential cause. Typically, transmittance measurements can be supported by complementary luminescence measurements. This is not possible in the case of ion-implanted samples, since the vast

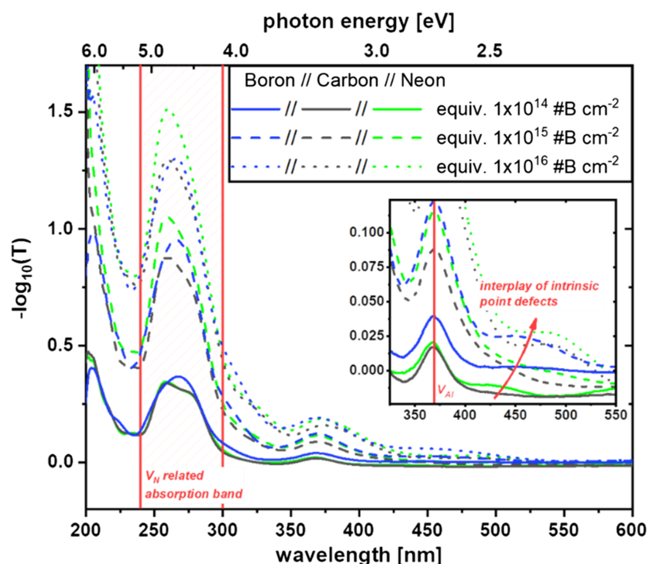

Figure 4. Measured absorbance spectra of all three different implantation series. The data was referenced to a non-implanted sample to suppress thin film fringes. The spectra show two distinct bands with transmittance losses that can be related to V_{Al} and most probably V_N.

amount of defects quench all potential luminescence even under heavy electron irradiation in a cathodoluminescence setup. Before the transmittance results are analyzed in more detail, a brief remark concerning the relation between absorbance and transmittance should be made. In our experiment, we are measuring transmittance. A loss of transmission, however, is a sum of absorption and reflection. Therefore, our experimental measurement is given as $Y = \log_{10}(I_0/I_{\text{transmitted}}) = -\log_{10}(T)$.[26] Thus, a value of $Y = 1$ means that 90% of the received photons do not reach the detector. Since the loss channels may be either absorption or reflection and thus absorbance as an axis labeling may be misleading, the vertical axis is labeled as $-\log_{10}(T)$. Still, for purpose of ease, the measured signal will be referred to as absorbance

© 2022 The Authors. physica status solidi (a) applications and materials science published by Wiley-VCH GmbH

18626319, 0, Downloaded from https://onlinelibrary.wiley.com/doi/10.1002/pssa.202200485 by Cochrane Germany, Wiley Online Library on [11/05/2023]. See the Terms and Conditions (https://onlinelibrary.wiley.com/terms-and-conditions) on Wiley Online Library for rules of use; OA articles are governed by the applicable Creative Commons License

hereinafter, where "loss of transmittance" would be more precise. As a second remark, if one would use the (in this case physically incorrect[26]) well-known and often-used expression derived from the Lambert–Beer law, the calculated absorption coefficient for B1E14 to B1E16 would yield values between 30.000 and 100.000 cm^{-1} at ≈4.7 eV, respectively.

To suppress thin film fringes that complicate the identification of absorption or reflection components, an as-deposited sample from the same process was used as the reference sample for the measurement of I_0.

We would like to highlight the excellent agreement between the absorbance of the boron and carbon implanted samples for implantations with a nominally identical concentration of intrinsic point defects, as shown in Figure 4. These results demonstrate the power of TRIM to predict damage profiles after implantation experiments.[27] Nonetheless, the neon implanted sample shows slightly stronger absorbance. This may be attributed to the fact that the calculated adjustment factors are not exact and that the Ne defect profile is slightly different, as seen in Figure 1b for higher depths.

In addition to the dominant 265 nm absorption band, Figure 4 reveals a distinct second absorbance peak at 370 nm/3.35 eV for the as-implanted samples. The second peak can likely be attributed to V_{Al}, which was predicted by theoretical calculations to yield an absorption at 3.4 eV.[28] It was also observed in proton- and neutron-irradiated samples.[29,30] Recently, Cardoso et al. implanted Eu into AlN and measured two excitation bands at 270 and 367 nm, which agrees excellently with our measured absorption bands.[31] A lower intensity in absorption for V_{Al} is also in line with our TRIM results, referring to the calculated vacancy ratio of 2.4. In our measurements, both bands rise in intensity with increasing implantation fluence, thus higher intrinsic point defect density in the sample. The broad and steady increase of absorption in the visible spectral range up to a wavelength of 550 nm may be attributed to an interplay between intrinsic point defects, since it can be observed in all samples independently from the implantation species. This broad absorption band is the reason for the amber-colored appearance of the samples. We also want to point out that extended defects like randomly oriented domains or localized stacking faults (i.e., dislocation loops) are unlikely to be the source of any significant absorption, since AlN is known for not showing these features even at high implantation fluences of 4×10^{16} cm^{-2}.[16]

Regarding the strong absorption that is centered at 265 nm, we now want to refute the established interpretation in the literature that attributes this distinct absorption solely to carbon impurities on nitrogen sites. Since the 265 nm absorption can be observed in samples grown with different kinds of techniques like PVT, MOVPE as well as hydride vapour phase epitaxy and was now additionally reported in implantation experiments with different species including but not limited to carbon, we want to conclude that intrinsic point defects (most likely V_N) are strongly involved in this absorption and the real role of carbon may need to be revised. A comprehensive model for this will be suggested in the subsequent section, which is based on DFT calculations published over the past decade. These existing calculations from the last years will be reviewed and critically checked against the new model.

Transmittance spectra measured after HTA for samples with all three different implant species are shown in **Figure 5**. After HTA, the strong absorption bands, which were prominently seen in the as-implanted samples, are no longer visible. For all three types of implant species and fluences, the transmittance spectra after HTA show no distinct absorption in the ranges discussed above. After annealing, the boron and neon series both exhibit similar spectra compared to the as-grown, non-implanted, and annealed reference sample. Like the boron and neon implant series, the carbon series shows no distinct absorption around 265 nm, but interestingly a drop of transmittance in the deeper UV-C down to the wavelength of fundamental bandgap absorption. Furthermore, this absorption increases with increasing implantation fluence, i.e., the concentration of carbon impurities. This result underlines that C_N is indeed involved in optical transitions causing absorption losses in the UV-C range.

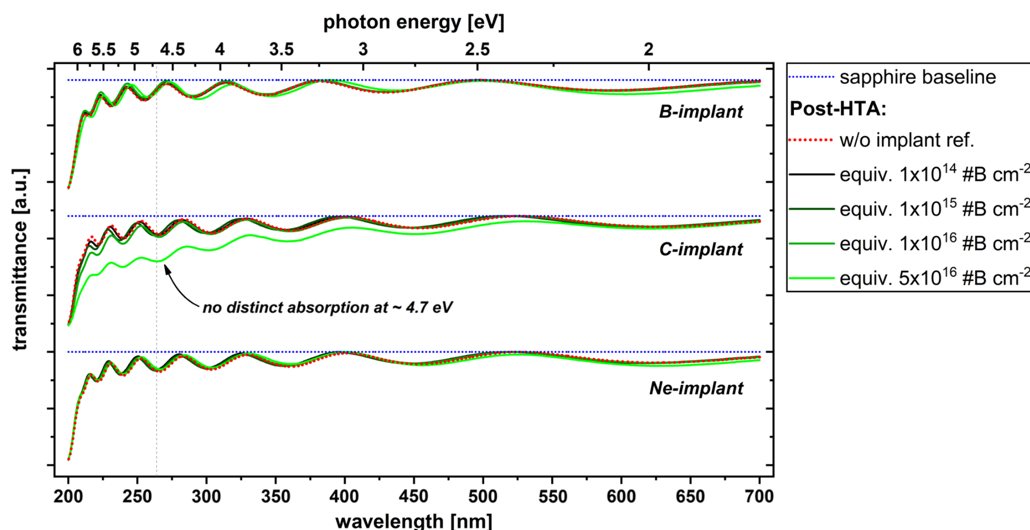

Figure 5. Transmittance spectra for all three different implantation series after high-temperature annealing (HTA). The measured data is referenced to a bare sapphire wafer. For the carbon series, one can observe a steady decrease of the transmittance below 250 nm for the lower fluences and a drastic deterioration of the optical quality for the highest fluence up to the red spectral range.

© 2022 The Authors. physica status solidi (a) applications and materials science published by Wiley-VCH GmbH

18626319, 0, Downloaded from https://onlinelibrary.wiley.com/doi/10.1002/pssa.202200485 by Cochrane Germany, Wiley Online Library on [11/05/2023]. See the Terms and Conditions (https://onlinelibrary.wiley.com/terms-and-conditions) on Wiley Online Library for rules of use; OA articles are governed by the applicable Creative Commons License

However, it does not seem to be the exclusive cause of the ≈4.7 eV absorption band, but rather may be responsible for a broader range of optical transitions, potentially involving other extrinsic impurities or intrinsic defects. The sample with the highest carbon concentration shows a steady decrease of transmittance towards smaller wavelengths, already setting in in the red spectral range. Consistently to the transmittance data, the sample with the highest carbon concentration shows a gray–green coloring to the human eye after HTA. For this sample, the HTA either was not able to recover all the implantation damage, or high-carbon concentrations may lead to a wide range of different energetic transitions inside the bandgap due to carbon-related disorder or point defect states.

In the following, a model is suggested that further supports the statement of V_N being involved in the UV-C absorption consistently to observations in different experiments in the literature. The argumentation is based on defect formation energy calculations published over the past decade. In all samples described in the literature, the measured density of carbon impurities scales with the UV-C absorption, as long as oxygen or silicon (both donor-type defects) are lower in concentration.[3–5,23,32] Thus, a correspondence between C and Si/O seems to exist. Especially in Al-rich growth conditions, carbon incorporates as an acceptor on nitrogen sites (C_N).[2,8,33] With an increasing concentration of C_N, the Fermi level decreases towards the valence band, leading to a reduction in the formation energy of compensating donors. Compensation can be accomplished by donor-type impurities like oxygen and silicon, or by the formation of the right type of intrinsic point defects with donor character, e.g., V_N. Gaddy et al. calculated that in the presence of carbon, V_N will occur as a compensating donor under Al-rich to balanced growth conditions.[8] Especially in Al-rich conditions, the concentrations of V_N and C_N converge.[8] In N-rich conditions, C_N will be compensated mostly by C_{Al} in the absence of other donor-type species, e.g., oxygen or silicon. Experimentally, quenching of ≈4.7 eV absorption via Si incorporation was shown by Gaddy et al.[12] This behavior is a consequence of the amphoteric nature of carbon in AlN, since both C_N and C_{Al} have comparable formation energies with E_{Form} of C_{Al} being lower than for V_N under these conditions.[2,8,33] For example, for MOVPE-grown layers, it was already reported that low supersaturations, e.g., obtained by pulsed growth modes that include Al-rich growth phases, lead to prominent absorption around 265 nm.[4] Assuming that every AlN crystal that incorporates only carbon impurities forms V_N as a compensating defect, the experimental results from the former literature are still consistent with our interpretation of V_N as the potential source of the UV-C absorption. Since the formation energy of O_N is lower than for V_N in N- and Al-rich growth conditions for all positions of E_F in the bandgap[28] (there are also calculations showing a lower formation energy for V_N than for O_N at $E_F < 1$ eV[9]), one has to expect a decrease of the intensity of the distinct absorption band around 265 nm as soon as oxygen is incorporated, if its origin is in fact V_N. This effect was indeed already described in literature several times for PVT growth.[5,10,11,34] Furthermore, Hartmann et al. found an empirical relation between carbon and donor-type impurities to achieve transparent crystals.[5] Additionally, we want to give a counterargument to the occasionally stated hypothesis that the n-type behavior of oxygen-doped AlN leads to quenching of the former carbon-related absorption, as suggested by Irmscher et al.:[24] Since our samples do not show the 265 nm absorption band before implantation, the reduced transmittance in the given range after boron and neon implantation cannot be a result from carbon impurities in the first place. We presume that the absorption of the ion-implanted samples is reduced during HTA of AlN on sapphire by two effects: First, annealing of the excess intrinsic point defects, i.e., Frenkel pairs at comparably low temperatures, and second, diffusion from oxygen into the AlN that tends to occupy the nitrogen vacancies due to the lower formation energy of O_N compared to V_N.[19,28] As a last argument, even the absence

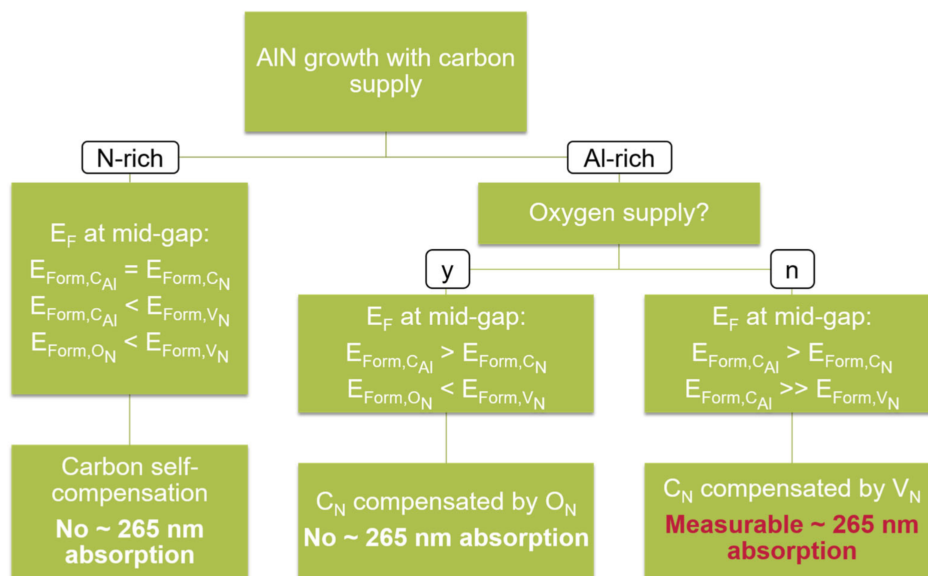

Figure 6. Suggested model for management of the 265 nm absorption band during AlN growth based on density functional theory (DFT) calculations and experimental results from the literature.[2,5,8,9,12,24,28,33,35]

© 2022 The Authors. physica status solidi (a) applications and materials science published by Wiley-VCH GmbH

18626319, 0, Downloaded from https://onlinelibrary.wiley.com/doi/10.1002/pssa.202200485 by Cochrane Germany, Wiley Online Library on [11/05/2023]. See the Terms and Conditions (https://onlinelibrary.wiley.com/terms-and-conditions) on Wiley Online Library for rules of use; OA articles are governed by the applicable Creative Commons License

of the 265 nm absorption in N-richer growth conditions shown by Tillner et al. fits this model, since the amphoteric nature of carbon leads to self-compensation with reduced V_N formation, as stated earlier and simulated by Gaddy et al.[4,8] Finally, the whole argumentation follows calculations and results that were already available in the literature. Only the addition of this new set of experiments, i.e., ion implantation as a means of controllably introducing carbon impurities and purposefully creating vacancy-type defects in high-quality AlN using optically inactive reference species, enables a deeper understanding of the fundamental nature of the 265 nm absorption band.

As a guidance, the relation between formation energies and interplay of point defects regarding their compensation described earlier is simplified in the flowchart in **Figure 6**, which shows the case for an idealized experiment: The amphoteric nature of carbon impurities in AlN leads to self-compensation, as long as growth happens in nitrogen-rich conditions due to the similar formation energies of C_{Al} and C_N and the lower formation energy of C_{Al} compared to V_N. In aluminum-rich conditions, the formation energy of C_{Al} increases relatively to the formation energy of V_N and O_N. If no oxygen is supplied, this leads to the compensation of the acceptor C_N with the intrinsic point defect V_N. Contrary, as soon as enough oxygen is supplied during growth, the acceptor C_N is mainly compensated by the donor with the lowest formation energy O_N. As soon as enough oxygen is incorporated, none or merely a suppressed absorption around $\approx$4.7 eV is measurable.

To conclude, the authors concede that pinpointing the exact mechanism for the occurrence of the $\approx$4.7 eV absorption band in AlN is indeed very challenging due to the tight connection between C_N as an acceptor-type defect and its potential compensator V_N. Our results indicate that a distinct absorption centered at $\approx$4.7 eV may also be caused by intrinsic defects introduced during ion implantation with different species, irrespective of the carbon concentration. Further, purposefully designed experiments are necessary to properly distinguish the effects of C_N and V_N on the optical properties of AlN crystals. In light of the reported findings, a critical reexamination of the origin of the $\approx$4.7 eV absorption band may be necessary.

3. Conclusions

Our experiments imply that intrinsic point defects can be fully recovered during HTA of AlN thin films grown on sapphire substrates. The observations suggest that the 265 nm absorption may be caused by V_N rather than C_N as commonly assumed in literature until now. Concurrently, the experimental design provides new insights into the 265 nm absorption band of AlN crystals and opens the interpretation of UV absorption for a revision. Transmittance measurements, combined with specially tailored implantation experiments based on Monte Carlo simulations allowed to identify that intrinsic point defects play a major role in this absorption band. Finally, we suggested a full model for the formation of V_N and its role in deep UV absorption in AlN in the presence of typical, hard to avoid impurities, oxygen and carbon.

4. Experimental Section

Nominally 300 nm thick commercial AlN samples fabricated by PVD on *c*-oriented sapphire substrates have been used for all experiments. The as-grown samples exhibit a nanocolumnar morphology with *c*-oriented, Al-polar grains. XRD rocking curve full width at half maximums for the (0002) and (10-12) reflex of $\approx$200 arcsec and $\approx$2500 arcsec, respectively, indicate highly *c*-oriented crystallites. Even though the twist angle of PVD AlN is comparably high, such films are still single-crystalline in nature.[36] Typically, sputtered AlN templates can be used as nucleation layers for GaN buffers with low screw- and mixed-type dislocation densities. To ascertain the best possible comparability, samples from the same deposition runs were used for the same implantation species. For planning the different implantation experiments, the freely available software package TRIM ("Transport of Ions in Matter") was employed. The Monte Carlo simulation TRIM is based on a binary collision approximation between the implanted species and the atoms of the target material.

In addition to the normalized implant species distributions, TRIM also calculates the amount of vacancy defects generated per unit length per implanted ion. The profiles shown in this publication were calculated using 10^4 single implantation events. The mathematics and theory of TRIM, i.e., Monte Carlo simulations and ion implantation are described in detail elsewhere.[37]

Boron (B^+) ions were implanted into full 2" AlN-on-sapphire wafers in a commercial Varian ViiSta HCS system using BF_3 as a source by repeatedly moving the samples through the ion beam with a top-hat profile. The boron implantations were performed with an acceleration voltage of 40 kV. Neon (70 keV) and carbon (47.5 keV) ions were implanted into 18×18 mm samples by scanning the ion beam across the sample. The samples were tilted by 6° to 7° with respect to the incident ion beam to avoid channeling phenomena.

The HTA was carried out inside a cold-wall vacuum furnace, using an N_2 atmosphere at ambient pressure. All components inside the furnace consist of porous Al_2O_3 (thermal isolation), sintered Al_2O_3 (tube, sampleholder), AlN (oxygen getter), and molybdenum (heater). Thus, annealing takes place in a low-oxygen, pure N_2 atmosphere. The samples were annealed in a face-to-face configuration to suppress thermal decomposition.[18,38] After loading, the furnace was evacuated to 50 mbar and purged three times with pure N_2. After reaching 200 °C, the atmosphere was changed additionally two times to reduce moisture content. Subsequently, the temperature controller was set to 1700 °C with a maximum heating rate of 8 K min^{-1} and dwell time of 3 h after reaching T_{dwell}. After three hours of dwell time, the heater was turned off and the samples cooled passively, while purged with 5 slm of N_2 during heating and cooling.

To obtain information on the optical characteristics of the as-grown, as-implanted, and high-temperature-annealed samples, transmittance measurements were carried out using a JASCO V-670 UV–vis spectrometer. The transmitted light was collected using an integrating sphere mounted into the spectrometer. The data was acquired using a bandwidth of 0.1 nm and a scan speed of 100 nm min^{-1}. If not described differently, bare sapphire wafers were used as a reference sample for the transmittance measurements.

The structural quality of the AlN layers after implantation and HTA were analyzed using a Panalytical X'Pert Pro HRXRD setup. The extent of crystal damage resulting in the presence of a strained layer and disordering was derived from coupled ω-2θ scans of the symmetric (0002) reflex and reciprocal space maps of the symmetric (0002) and asymmetric (10–15) and (−1015) reflexes. In addition, the structural quality of the layers was assessed by acquiring ω-scans (rocking curves) of several AlN reflexes in symmetric and skew-symmetric geometry.[39]

Acknowledgements

L.P. and C.M. contributed equally to this work. This work was funded by Deutsche Forschungsgemeinschaft (DFG) in the framework of the SPP 2312 (Energieeffiziente Leistungselektronik "GaNius"), Project No. 462737320 (Aluminium Nitrid für die vertikale Leistungselektronik). The authors also thank Patrick Hoffmann for his technical assistance on the implantations.

Open Access funding enabled and organized by Projekt DEAL.

© 2022 The Authors. physica status solidi (a) applications and materials science published by Wiley-VCH GmbH

18626319, 0, Downloaded from https://onlinelibrary.wiley.com/doi/10.1002/pssa.202200485 by Cochrane Germany, Wiley Online Library on [11/05/2023]. See the Terms and Conditions (https://onlinelibrary.wiley.com/terms-and-conditions) on Wiley Online Library for rules of use; OA articles are governed by the applicable Creative Commons License

Conflict of Interest

The authors declare no conflict of interest.

Author Contributions

C.M.: performed parts of the simulations, HRXRD measurements, processing of the data, and took an active part in the writing of this article; L.P.: performed the annealing experiments, parts of the simulations, transmittance measurements, processing of the data, and took an active part in the writing of this article; C.R.: performed parts of the implantation experiments; J.K.: performed parts of the implantation experiments; A.W.: acquired the funding for this project and supervised this research. All authors contributed to the discussion and writing of the article.

Data Availability Statement

The data that support the findings of this study are available from the corresponding author upon reasonable request.

Keywords

absorption, AlN, carbon, high-temperature annealing, ion implantation, point defects, transmittance

Received: July 15, 2022
Revised: September 2, 2022
Published online:

[1] M. Kneissl, T. Y. Seong, J. Han, H. Amano, *Nat. Photonics* **2019**, *13*, 233.
[2] R. Collazo, J. Xie, B. E. Gaddy, Z. Bryan, R. Kirste, M. Hoffmann, R. Dalmau, B. Moody, Y. Kumagai, T. Nagashima, Y. Kubota, T. Kinoshita, A. Koukitu, D. L. Irving, Z. Sitar, *Appl. Phys. Lett.* **2012**, *100*, 191914.
[3] T. Nagashima, Y. Kubota, T. Kinoshita, Y. Kumagai, J. Xie, R. Collazo, H. Murakami, H. Okamoto, A. Koukitu, Z. Sitar, *Appl. Phys. Express* **2012**, *5*, 125501.
[4] N. Tillner, C. Frankerl, F. Nippert, M. J. Davies, C. Brandl, R. Lösing, M. Mandl, H. J. Lugauer, R. Zeisel, A. Hoffmann, A. Waag, M. P. Hoffmann, *Phys. Status Solidi B* **2020**, *257*, 2000278.
[5] C. Hartmann, J. Wollweber, S. Sintonen, A. Dittmar, L. Kirste, S. Kollowa, K. Irmscher, M. Bickermann, *CrystEngComm* **2016**, *18*, 3488.
[6] D. D. Koleske, A. E. Wickenden, R. L. Henry, M. E. Twigg, *J. Cryst. Growth* **2002**, *242*, 55.
[7] M. Bickermann, B. M. Epelbaum, O. Filip, B. Tautz, P. Heimann, A. Winnacker, *Phys. Status Solidi C* **2012**, *9*, 449.
[8] B. E. Gaddy, Z. Bryan, I. Bryan, R. Kirste, J. Xie, R. Dalmau, B. Moody, Y. Kumagai, T. Nagashima, Y. Kubota, T. Kinoshita, A. Koukitu, Z. Sitar, R. Collazo, D. L. Irving, *Appl. Phys. Lett.* **2013**, *103*, 161901.
[9] D. Alden, J. S. Harris, Z. Bryan, J. N. Baker, P. Reddy, S. Mita, G. Callsen, A. Hoffmann, D. L. Irving, R. Collazo, Z. Sitar, *Phys. Rev. Appl.* **2018**, *9*, 054036.
[10] C. Hartmann, A. Dittmar, J. Wollweber, M. Bickermann, *Semicond. Sci. Technol.* **2014**, *29*, 084002.
[11] R. R. Sumathi, *ECS J. Solid State Sci. Technol.* **2021**, *10*, 035001.
[12] B. E. Gaddy, Z. Bryan, I. Bryan, J. Xie, R. Dalmau, B. Moody, Y. Kumagai, T. Nagashima, Y. Kubota, T. Kinoshita, A. Koukitu, R. Kirste, Z. Sitar, R. Collazo, D. L. Irving, *Appl. Phys. Lett.* **2014**, *104*, 202106.
[13] L. Jin, K. Zhao, S. Xu, Z. Qin, H. Cheng, L. Zhang, H. Qi, J. Li, R. Zheng, H. Wu, *Scr. Mater.* **2021**, *190*, 91.
[14] J. Xi, B. Liu, Y. Zhang, W. J. Weber, *J. Appl. Phys.* **2018**, *123*, 045904.
[15] E. Wendler, W. Wesch, *Nucl. Instrum. Methods Phys. Res., Sect. B* **2006**, *242*, 562.
[16] W. Jiang, I. T. Bae, W. J. Weber, *J. Phys.: Condens. Matter* **2007**, *19*, 356207.
[17] H. Fukuyama, H. Miyake, G. Nishio, S. Suzuki, K. Hiramatsu, *Jpn. J. Appl. Phys.* **2016**, *55*, 05FL02.
[18] H. Miyake, C. H. Lin, K. Tokoro, K. Hiramatsu, *J. Cryst. Growth* **2016**, *456*, 155.
[19] T. Pornphatdetaudom, T. Yano, K. Yoshida, *Nucl. Mater. Energy* **2018**, *16*, 24.
[20] R. Kirste, B. Sarkar, P. Reddy, Q. Guo, R. Collazo, Z. Sitar, *J. Mater. Res.* **2021**, *36*, 1.
[21] L. Y. Li, K. Shima, M. Yamanaka, K. Kojima, T. Egawa, A. Uedono, S. Ishibashi, T. Takeuchi, M. Miyoshi, S. F. Chichibu, *Appl. Phys. Lett.* **2021**, *119*, 091105.
[22] R. Yu, G. Liu, G. Wang, C. Chen, M. Xu, H. Zhou, T. Wang, J. Yu, G. Zhao, L. Zhang, *J. Mater. Chem. C* **2021**, *9*, 1852.
[23] I. Gamov, C. Hartmann, J. Wollweber, A. Dittmar, T. Straubinger, M. Bickermann, I. Kogut, H. Fritze, K. Irmscher, *J. Appl. Phys.* **2019**, *126*, 215102.
[24] K. Irmscher, C. Hartmann, C. Guguschev, M. Pietsch, J. Wollweber, M. Bickermann, *J. Appl. Phys.* **2013**, *114*, 123505.
[25] H. Amano, R. Collazo, C. De Santi, S. Einfeldt, M. Funato, J. Glaab, S. Hagedorn, A. Hirano, H. Hirayama, R. Ishii, Y. Kashima, Y. Kawakami, R. Kirste, M. Kneissl, R. Martin, F. Mehnke, M. Meneghini, A. Ougazzaden, P. J. Parbrook, S. Rajan, P. Reddy, F. Römer, J. Ruschel, B. Sarkar, F. Scholz, L. J. Schowalter, P. Shields, Z. Sitar, L. Sulmoni, T. Wang, et al., *J. Phys. D. Appl. Phys.* **2020**, *53*, 503001.
[26] T. G. Mayerhöfer, H. Mutschke, J. Popp, *ChemPhysChem* **2016**, *17*, 1948.
[27] M. I. Bratchenko, V. V. Bryk, S. V. Dyuldya, A. S. Kalchenko, N. P. Lazarev, V. N. Voyevodin, *Probl. At. Sci. Technol.* **2013**, *11*, 11.
[28] Q. Yan, A. Janotti, M. Scheffler, C. G. Van De Walle, *Appl. Phys. Lett.* **2014**, *105*, 111104.
[29] K. Atobe, M. Honda, N. Fukuoka, M. Okada, M. Nakagawa, *Jpn. J. Appl. Phys.* **1990**, *29*, 150.
[30] J. M. Mäki, I. Makkonen, F. Tuomisto, A. Karjalainen, S. Suihkonen, J. Räisänen, T. Y. Chemekova, Y. N. Makarov, *Phys. Rev. B: Condens. Matter Mater. Phys.* **2011**, *84*, 081204(R).
[31] J. P. S. Cardoso, M. R. Correia, R. Vermeersch, D. Verheij, G. Jacopin, J. Pernot, T. Monteiro, S. Cardoso, K. Lorenz, B. Daudin, N. Ben Sedrine, *ACS Appl. Nano Mater.* **2022**, *5*, 972.
[32] C. Hartmann, L. Matiwe, J. Wollweber, I. Gamov, K. Irmscher, M. Bickermann, T. Straubinger, *CrystEngComm* **2020**, *22*, 1762.
[33] J. L. Lyons, A. Janotti, C. G. Van De Walle, *Phys. Rev. B: Condens. Matter Mater. Phys.* **2014**, *89*, 035204.
[34] Q. Wang, D. Lei, G. He, J. Gong, J. Huang, J. Wu, *Phys. Status Solidi Appl. Mater. Sci.* **2019**, *216*, 1900118.
[35] Q. Zhou, Z. Zhang, H. Li, S. Golovynskyi, X. Tang, H. Wu, J. Wang, B. Li, *APL Mater.* **2020**, *8*, 081107.
[36] L. Cancellara, S. Hagedorn, S. Walde, D. Jaeger, M. Albrecht, *J. Appl. Phys.* **2022**, *131*, 215304.
[37] J. F. Ziegler, J. P. Biersack, M. D. Ziegler, *SRIM - The Stopping and Range of Ions in Matter*, SRIM Co., Chester, MD, USA **2008**.
[38] H. Fujino, E. Kume, S. Sakai, *Phys. C: Supercond. Appl.* **2005**, *426–431*, 1474.
[39] S. R. Lee, A. M. West, A. A. Allerman, K. E. Waldrip, D. M. Follstaedt, P. P. Provencio, D. D. Koleske, C. R. Abernathy, *Appl. Phys. Lett.* **2005**, *86*, 241904.

© 2022 The Authors. physica status solidi (a) applications and materials science published by Wiley-VCH GmbH

18626319, 0, Downloaded from https://onlinelibrary.wiley.com/doi/10.1002/pssa.202200485 by Cochrane Germany, Wiley Online Library on [11/05/2023]. See the Terms and Conditions (https://onlinelibrary.wiley.com/terms-and-conditions) on Wiley Online Library for rules of use; OA articles are governed by the applicable Creative Commons License